

The treasure behind the haystack: MUSE analysis of five recently discovered globular clusters[★]

F. Gran^{1,2,3}, G. Kordopatis¹, M. Zoccali^{2,3}, V. Hill¹, I. Saviane⁴, C. Navarrete^{1,4}, A. Rojas-Arriagada^{5,3,6,7},
J. Carballo-Bello⁸, J. Hartke^{9,10}, E. Valenti¹¹, R. Contreras Ramos³, M. De Leo^{2,3}, and S. Fabbro^{1,12}

¹ Université Côte d’Azur, Observatoire de la Côte d’Azur, CNRS, Laboratoire Lagrange, Nice, France, e-mail: fgran@oca.eu

² Instituto de Astrofísica, Av. Vicuña Mackenna 4860, Santiago, Chile

³ Millennium Institute of Astrophysics, Av. Vicuña Mackenna 4860, 82-0436 Macul, Santiago, Chile

⁴ European Southern Observatory, Alonso de Córdova 3107, Casilla 19001 Santiago, Chile

⁵ Departamento de Física, Universidad de Santiago de Chile, Av. Victor Jara 3659, Santiago, Chile

⁶ Núcleo Milenio ERIS

⁷ Center for Interdisciplinary Research in Astrophysics and Space Exploration (CIRAS), Universidad de Santiago de Chile, Santiago, Chile

⁸ Instituto de Alta Investigación, Universidad de Tarapacá, Casilla 7D, Arica, Chile

⁹ Finnish Centre for Astronomy with ESO (FINCA), FI-20014 University of Turku, Finland

¹⁰ Tuorla Observatory, Department of Physics and Astronomy, FI-20014 University of Turku, Finland

¹¹ European Southern Observatory, Karl Schwarzschild-Strabe 2, 85748 Garching bei München, Germany

¹² National Research Council of Canada, Herzberg Astronomy & Astrophysics Research Centre, 5071 West Saanich Road, Victoria, BC V9E 2E7, Canada

Received ; accepted

ABSTRACT

Context. After the second data release of Gaia, the number of new globular cluster candidates has increased importantly. However, most of them need to be properly characterised, both spectroscopically and photometrically, by means of radial velocities, metallicities, and deeper photometric observations.

Aims. Our goal is to provide an independent confirmation of the cluster nature of Gran 4, a recently discovered globular cluster, with follow-up spectroscopic observations. The derived radial velocity for individual stars, coupled with proper motions, allows us to isolate cluster members from field stars, while the analysis of their spectra allows us to derive metallicities. By including in the analysis the recently confirmed clusters Gran 1, 2, 3, and 5, we aim to completely characterise the sample presented in Gran et al. 2022.

Methods. Using Gaia DR3 and VVV catalogue data and MUSE@VLT observations, we performed a selection of cluster members based on their proper motions, radial velocities and their position in colour-magnitude diagrams. Furthermore, full spectral synthesis was performed on the cluster members, extracting surface parameters and metallicity from MUSE spectra. Finally, a completeness estimation was performed on the total globular cluster population of the Milky Way.

Results. We confirm the nature of Gran 4, a newly discovered globular cluster behind the Galactic bulge, with a mean radial velocity of $RV = -265.28 \pm 3.92 \text{ km s}^{-1}$ and a mean metallicity of $[Fe/H] = -1.72 \pm 0.32 \text{ dex}$. Additionally, independent measurements of the metallicities were derived for Gran 1, 2, 3, and 5. We also revise the observational lower mass limit for a globular cluster to survive in the bulge/disk environment. We estimate that $\sim 12 - 26$ globular clusters have still to be discovered on the other side of the Galaxy (i.e., behind the bulge/bar/disk), up to 20 kpc.

Key words. Surveys – Stars: kinematics and dynamics – Galaxy: bulge – Galaxy: halo – globular clusters: general – Proper motions

1. Introduction

Globular clusters (GCs) are dense agglomerations of gravitationally bound stars formed roughly at the same epoch and constitute an essential part of galaxies over the whole mass range (Brodie & Strader 2006). Although the details of the GC formation process are not yet completely understood (Renzini 2017; Forbes et al. 2018), significant progress has been made during the last years to connect high-redshift observations (Vanzella et al. 2017) with the Milky Way (MW) GC population (Gratton et al. 2004).

Historically, GCs have been used as a crucial stellar laboratory given that distances, masses and approximate ages can be derived from their stellar populations (Bastian & Lardo 2018). Most of our understanding of stellar evolution comes from the analysis of star clusters (either GCs or open clusters, OCs; Gratton et al. 2019, and references therein), in which the European Space Mission Gaia (Gaia Collaboration et al. 2016) satellite has made a revolutionary contribution to our overall understanding of the MW cluster population (Bragaglia 2018; Choi et al. 2018; Cantat-Gaudin et al. 2020; Cantat-Gaudin 2022).

Given their old ages (mostly $\gtrsim 10$ Gyr), GCs are considered fossil records of the evolution of their host galaxy (Harris & Racine 1979; Recio-Blanco 2018), particularly Marín-Franch et al. (2009), Forbes & Bridges (2010) and Leaman et al. (2013)

[★] Based on observations collected at the European Southern Observatory under ESO programmes 0103.D-0386(A) and 105.20MY.001 (PI: F. Gran).

first used the MW GC age-metallicity relation to discriminate between accreted and in-situ objects. More recently, GCs have been used to identify merging events in the MW mass assembly history (Kruijssen et al. 2019a,b; Myeong et al. 2019; Massari et al. 2019; Callingham et al. 2022; Hammer et al. 2023, and references therein). Nonetheless, Pagnini et al. (2022) emphasise the presence of a significant overlap in the kinematic space between potentially accreted and in-situ objects.

The last few years have seen an important increase in the discovery of OCs (Castro-Ginard et al. 2018; Cantat-Gaudin et al. 2019; Castro-Ginard et al. 2020; He et al. 2021; Hunt & Reffert 2021; Castro-Ginard et al. 2022; He et al. 2022, 2023; Hunt & Reffert 2023) and GCs (Koposov et al. 2017; Gran et al. 2019; Garro et al. 2020; Huang & Koposov 2021; Garro et al. 2022a,b; Gran et al. 2022), thanks to the proper motions (PMs) measured by the Gaia satellite. Some new clusters were also discovered towards the Galactic bulge, even if the stellar extinction and crowding place a veil on the Gaia optical observations. However, most of these discoveries still need to be confirmed with radial velocities (RVs), deeper photometric observations, or even PM analysis. As shown in Cantat-Gaudin & Anders (2020) and Gran et al. (2019), the study of PMs has ruled out most of the cluster candidates proposed in the literature. To date, the total number of confirmed GCs in the MW is around 170 (Baumgardt & Vasiliev 2021; Vasiliev & Baumgardt 2021).

Gran et al. (2022) identified five new GCs towards the MW bulge, namely Gran 1, 2, 3, 4, and 5. They showed clustered PMs and well-defined evolutionary sequences in the colour-magnitude diagram (CMD). All of them were followed up spectroscopically to derive RV and metallicity measurements, unambiguously confirming the nature of Gran 1, 2, 3 and 5 (those with available data at the time of publication) in Gran et al. (2022). Positional, structural, and orbital parameters were also derived, showing that some of them lie on the other side of the bulge. The spectra for Gran 4 were obtained after the publication of that paper, and this is the reason we discuss them here. More recently, Pace et al. (2023) independently confirmed the GC nature of two of those clusters (Gran 3 and 4) using archival data and a follow-up spectroscopic campaign.

This article presents the measurements of RV and metallicity for stars in Gran 4 using MUSE data. The mean RV derived agrees well with recent studies. Our analysis complements the Pace et al. (2023) work, given that we precisely point at the inner 1 arcmin of each cluster at once. Additionally, the independently derived metallicity measurements for all the GCs presented in Gran et al. (2022), using low-resolution spectra that cover the complete optical regime (~ 5000 to ~ 9000 Å) is included.

The paper is organised as follows. Section 2 lists the used catalogues and surveys in this work, Section 3 describes the analysis of the low-resolution spectra acquired for this project and presents the RV of the newly discovered Gran 4. Section 4 elaborates on the observed low-mass limit of MW GCs according to their environment and provides an estimated number of missing GCs on the far side of the Galaxy (behind the Galactic bulge). Finally, Section 5 presents a discussion on the topic, the conclusions and prospects for this field.

2. Data and observations

We used the Gaia Data Release 3 (DR3, Gaia Collaboration et al. 2016, 2022) main catalogue to identify cluster members, extract optical magnitudes (Gaia G, BP, and RP), and proper motions ($\mu_\alpha \cos \delta$ and μ_δ). We recall that Gran et al. (2019) initially used the Gaia DR2 (Gaia Collaboration et al. 2018) to discover

Gran 1, 2, 3, 4, and 5, which we now update to the DR3 version for the present analysis.

In addition, deep near-IR J,K_s photometry from the VISTA Variables in the Vía Láctea survey (hereafter VVV; Minniti et al. 2010) was used to confirm the presence of stellar overdensities at the cluster centres and complement the optical photometry from Gaia. For VVV, we used the public catalogues provided in Surot et al. (2019), in which point-spread function (PSF) photometry was extracted from stacked J and K_s images. The stacking process resulted in photometry that goes deeper than other similar catalogues (e.g.; Contreras Ramos et al. 2017; Smith et al. 2018) at the price of not including near-IR proper motions, nor light curves, for the faintest stars.

Finally, two follow-up observing campaigns with the Multi Unit Spectroscopic Explorer (MUSE; Bacon et al. 2010, R~1900-3700) mounted at the VLT-UT4 (Cerro Paranal, Chile) during ESO periods P103 and P105 were awarded to point at the discovered clusters. The MUSE integral field unit (IFU) allows us to observe a large number of stars (270-640 objects) in each field with a single pointing using the Wide Field Mode (WFM, one sq arcmin field-of-view). Additionally, we used the GALACSI adaptive optics system (Stuik et al. 2006; Ströbele et al. 2012; Hartke et al. 2020) to improve the spatial resolution, which is crucial for these crowded objects. Standard one-hour observing blocks (OBs) were executed between July 2019 and September 2021 with a typical image quality of $\sim 0.8 - 0.9$ arcsec per exposure. The processing of raw data was done by the automatic MUSE pipeline (Weilbacher et al. 2020), using standard calibrations, and the reduced datacubes were retrieved from the ESO User Portal. Note that MUSE wavelength values are calibrated using arc line wavelengths in standard air and a conversion must be done when transforming it into the vacuum reference frame (Weilbacher et al. 2020).

3. Analysis of the MUSE datacubes and confirmation of the GC Gran 4

3.1. Extraction and Analysis of MUSE spectra

We follow the procedure described in Gran et al. (2022) to extract stellar spectra from MUSE cubes; however, a few key modifications were made to the analysis pipeline. The derivation of stellar atmospheric parameters was improved to use the entire extracted spectrum from the MUSE cubes. We summarise here the extraction procedure and spectral analysis.

The stellar sources were selected in the *I*-band image, which was obtained by convolving the MUSE cubes with the wavelength transmission function of the filter. The same procedure was performed to obtain *V*- and *R*-band images that will be used later in the analysis. To derive RVs for the observed stars, flux for all the sources 5σ above the background level were extracted in the *I*-band images, for each slice of the MUSE cubes. The primary motivation of this threshold is to remove low signal-to-noise ratio (SNR) stars that will be present in the field of view with no reliable spectra. This task was performed using the associated *Astropy*¹ package, *photutils*² (Astropy Collaboration et al. 2013, 2018, 2022; Bradley et al. 2022). After all the available cube layers were extracted, we created individual stellar spectra from ~ 5000 to ~ 9000 Å. The entire wavelength range was used in the derivation of both RV and stellar atmospheric parameters.

¹ <https://www.astropy.org/>

² <https://photutils.readthedocs.io/en/stable/>

RVs for all the stars were calculated using the cross-correlation function implemented in the python package `doppler` (Nidever 2021). The package fits RV, T_{eff} , $\log g$, and $[\text{Fe}/\text{H}]$ at the same time, using a pre-computed grid of synthetic spectra. It is based on the data-driven code The Cannon (Ness et al. 2015) to derive the observed spectral features, whose phase-space was explored in a MCMC ensemble (Foreman-Mackey et al. 2013) to extract parameter uncertainties. Given the model flexibility and the large parameter space covered by the synthetic grid, horizontal branch (HB) stars with prominent Hydrogen lines were also fitted without major issues.

In order to ensure a proper calibration of the RVs and stellar atmospheric parameters derived by `doppler`, we used the AMBRE grid of synthetic spectra (de Laverny et al. 2012, 2013). Given that our science target is only GC giant stars, we limit the grid to a sub-sample of 456 spectra. We choose the grid limits based on the expected effective temperatures ($4250 \leq T_{\text{eff}} \text{ (K)} \leq 5250$, in steps of 250 K), surface gravities ($0 \leq \log g \text{ (dex)} \leq 3$, in steps of 0.5 dex), metallicities ($-3.0 \leq [\text{Fe}/\text{H}] \text{ (dex)} \leq -1$, in steps of 0.5 dex), and α -elements enhancement ($0.0 \leq [\alpha/\text{Fe}] \text{ (dex)} \leq 0.4$, in steps of 0.2 dex) of red giant stars in other GCs. Stars outside the cluster RGB, such as foreground disk stars, bulge dwarfs, or GC HB stars will present reliable RVs; however, their atmospheric parameters will not be considered here.

Overall, the derived RV, temperature, gravity and metallicity uncertainties were compatible with previous studies (Wang et al. 2022), for a given SNR and magnitude. Mean uncertainty values of the order of 10 km s^{-1} , 100 K, 0.35 dex, and 0.35 dex were found for RVs, temperatures, surface gravities, and metallicities. Figure 1 shows the spectra of a typical high-SNR giant star of our sample, with emphasis on the Magnesium b triplet (Mgb λ 5167, 5172, 5183) and Calcium Triplet (CaT; λ 8498, 8542, 8662) areas, as well as an HB star with prominent Hydrogen spectral features. Normalisation was achieved by `doppler` using a 6th order polynomial applied to the continuum pixels (i.e., percentile 90) after a $5\text{-}\sigma$ clipping. Table 1 contains all the coordinates and calibrated atmospheric parameters derived for each member star during this analysis (i.e., stars within the box in Figures 2 and A.1). Complete derived parameters for all clusters can be found in Appendix A, Table A.1 through Table A.5. Overall, we report here a more accurate measurement of the cluster parameters, lowering the error bars by a factor of ~ 2 in comparison with Gran et al. (2022). This change is directly related to the usage of the entire spectra instead of relying on the CaT region alone and its calibration to metallicity.

Using TOPCAT (Taylor 2005), *VRI*, Gaia DR3 and VVV data were added to the RV catalogue per cluster. This resulted in a catalogue of stars with measured tangential and line-of-sight (LOS) velocities (both PMs and RVs). We then selected cluster members based on the most prominent group of stars with coherent RVs, PMs and metallicities. We filter field stars using three times the RV dispersion (σ_{RV}) indicated in Table 2 as a threshold. The RV cuts implemented here ($3\sigma_{\text{RV}}$), agree with the maximum of observed dispersion in other MW GCs of $\leq 20 \text{ km s}^{-1}$ (Watkins et al. 2015). Metallicity selection constraints were flexible enough to account for their derived uncertainties (mean of ~ 0.35 dex), usually including outliers in the first selection. Subsequently, we iteratively reduce the selection limits, filtering field stars by their position in the Kiel diagram.

We confirmed the cluster nature of the five GCs analysed through this study. The final parameters for all the clusters presented in Gran et al. (2022) are listed in Table 2. Figure 2 shows the derived RVs, metallicities, and Kiel diagrams ($T_{\text{eff}}\text{-}\log g$)

for Gran 1 and 4. For completeness, in Appendix A the figures for the other three clusters (Gran 2, 3, and 5) can be found. In the case of Gran 1, RVs and metallicities are perfectly clumped in that plane, making the selection process straightforward. All the cluster stars belong to the RGB phase, for which the surface parameters are well calibrated, following the correct metallicity slope in the Kiel diagram. On the other hand, Gran 4 members are comprised of RGB, HB and possibly some sub-giant branch (SGB) or blue straggler (BS) stars, artificially spreading the metallicity values into a much wider range than expected for a mono-metallic GC (Bailin 2019; Bailin & von Klar 2022). We double-check our metallicity dispersions ($\sigma_{[\text{Fe}/\text{H}]}$) with the ones derived in Husser et al. (2020) for other MW GCs observed with MUSE, and for all but one cluster (Gran 4) their dispersion agrees with a mono-metallic stellar population. The larger $\sigma_{[\text{Fe}/\text{H}]}$ in Gran 4 can be explained by the lower SNR achieved for the cluster members, located at ~ 20 kpc, and also the relatively low number of measured RGB stars in the instrument field-of-view (15 RGB + 9 HB/SGB/BS stars).

As we mentioned earlier, we calibrated our AMBRE grid targeting only GC RGB stars, leaving other evolutionary stages without proper calibration. The calibration is evident when comparing the RGB sequence of the cluster with the 10 Gyr cluster mean metallicity PARSEC (Bressan et al. 2012; Marigo et al. 2013) isochrones. For this reason, the surface parameters derived from HB or SGB/BS stars (red crosses) are affected by more significant errors, as shown in Figure 2. Nonetheless, when selecting cluster RGB stars (green dots and hatched histogram), the spread is minor, allowing us to assign a mean metallicity of $[\text{Fe}/\text{H}] \sim -1.7$ to Gran 4, in perfect agreement with the results by Pace et al. (2023), that will be discussed in Section 5.

3.2. Confirmation of Gran 4

Given the well-defined sequences in the CMD of Gran 4, see Figure 3, and Gran et al. (2022), especially the extended HB and its low metallicity and RV, well outside the distribution of field stars, the identification of cluster members was straightforward. We used the 26 isolated spectroscopic members of Gran 4 and matched their coordinates (1 arcsec radius) into the Gaia DR3 catalogue. In total, 14 stars agree with the cluster RV and PM centroids. Considering individual measurement errors, we derive a weighted mean RV and metallicity of $-265.28 \pm 3.92 \text{ km s}^{-1}$ and -1.72 ± 0.32 dex, respectively, using 1σ uncertainties. These values agree with a mono-metallic stellar population, for which we can confirm that Gran 4 is indeed a real GC. Figure 3 shows the MUSE and Gaia-VVV CMDs for this cluster decontaminated from field stars by means of both PMs and RVs using optical and near-IR filters.

4. On the Milky Way globular cluster completeness and the initial mass limit of bulge globular clusters

4.1. Globular cluster completeness behind the Galactic bulge/plane

Recently, multiple efforts have been made to estimate the total number of GCs bound to the Galaxy and, consequently, the number of clusters still to be discovered within the MW. Usually, the main focus is given to the distant halo clusters (Contenta et al. 2017; Webb & Carlberg 2021, and references therein), assuming completeness of the GC population within Galactocentric distances confined to $R \leq 20 - 50$ kpc. Only a few studies have

Table 1. Stellar atmospheric parameters for MUSE selected Gran 1 members. Star ID, coordinates, temperature, surface gravity, metallicity, RV and mean SNR are presented for observed GC members. Only the first few rows are shown here, however, complete tables can be found in Table A.1 through A.5 within Appendix A.

GC - ID	RA (deg)	Dec (deg)	T_{eff} (K)	$\log g$ (dex)	[Fe/H] (dex)	RV (km s^{-1})	SNR
Gran 01 - 008	269.64794	-32.02559	4362	1.2	-1.17	68.25	133
Gran 01 - 017	269.64650	-32.02449	4659	1.4	-1.11	69.33	174
Gran 01 - 021	269.65005	-32.02420	4358	1.1	-1.14	75.04	241
Gran 01 - 022	269.65615	-32.02395	4611	1.4	-1.05	68.81	222

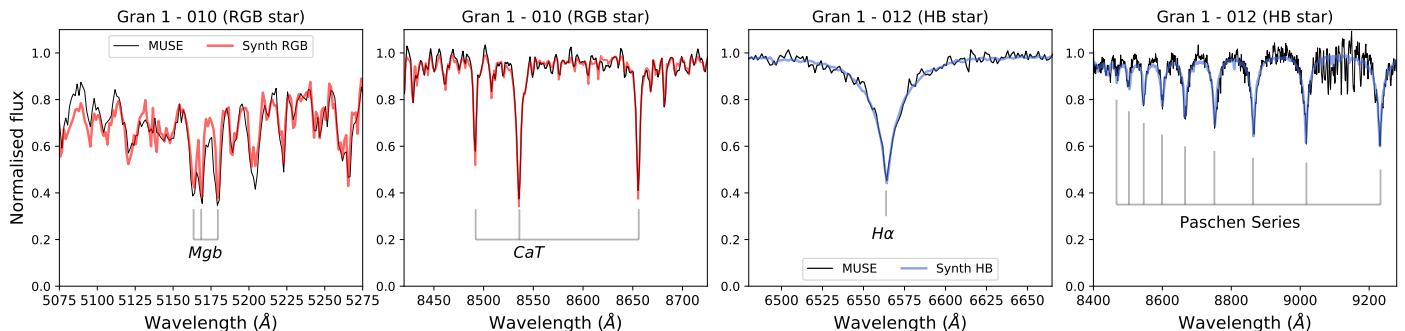


Fig. 1. Extracted MUSE spectra and associated models for different parts of the spectrum of two high-SNR (>110) stars: Gran 1 stars 010 and 012. In each panel, features in each region are highlighted. **Two left panels for RGB star, and two right panels for HB star:** Mgb around ~ 5175 Å, $H\alpha$ (6562 Å), CaT between $\sim 8400 - 8700$ Å, and the Paschen Hydrogen series starting at ~ 8450 Å.

Table 2. Structural and dynamical parameters derived for the analysed GCs. Name, coordinates (equatorial and Galactic), distance, mean RV, cluster observational velocity dispersion, median metallicity, mean PMs and the number of cluster member stars observed are included.

GC	RA (deg)	Dec (deg)	ℓ (deg)	b (deg)	d_{LOS} (kpc)	$RV \pm \sigma_{RV}$ (km s^{-1})	$[\text{Fe}/\text{H}] \pm \sigma_{[\text{Fe}/\text{H}]}$ (dex)	$\mu_{\alpha} \cos \delta$ (mas yr^{-1})	μ_{δ} (mas yr^{-1})	N_{stars}
Gran 1	269.651	-32.020	-1.233	-3.977	7.94	76.98 ± 3.62	-1.13 ± 0.06	-8.10	-8.01	43
Gran 2	257.890	-24.849	-0.771	8.587	16.60	61.24 ± 2.70	-1.46 ± 0.13	0.19	-2.57	28
Gran 3	256.256	-35.496	-10.244	3.424	10.50	91.57 ± 5.97	-1.63 ± 0.14	-3.74	0.71	33
Gran 4	278.113	-23.114	10.198	-6.388	21.90	-265.28 ± 3.92	-1.72 ± 0.32	0.51	-3.51	26
Gran 5	267.228	-24.170	4.459	1.838	4.47	-59.19 ± 4.93	-1.02 ± 0.11	-5.32	-9.20	42

questioned the completeness of the number of clusters on the other side of the Galaxy (Ryu & Lee 2018) or presented the detection and survival issues of GCs buried in the bulge (Minniti et al. 2017, 2021a).

The clusters presented in this work and other recently confirmed GCs in the inner MW (Garro et al. 2020; Pace et al. 2023) challenge the assumption of 100% completeness towards the Galactic bulge. In what follows, we will qualitatively estimate the number of missing GCs within Galactocentric distances smaller than 20 kpc and then combine that number with previous halo predictions. By adding Gran 4, RLGC 1 and 2, and Garro 1 (Ryu & Lee 2018; Garro et al. 2020) to the compilation by Baumgardt & Vasiliev (2021, March 2023 update), we can give first-order estimates of the missing GCs at the far side of the Galaxy. To do this, we consider and adopt the Galactic bar as a symmetry axis and assume that GCs are homogeneously distributed within the MW and that a Poisson distribution can model the number of GCs. This assumption is a first-order approximation of the observed GC distribution that exhibits a more complex structure (Arakelyan et al. 2018).

Figure 4 shows the adopted division to analyse the completeness of the GC population in four regions with an artistic representation of the Galaxy in the background³. In each of them (A, B, C and D), there are 58, 24, 31 and 31 known GCs, respec-

³ Image provided in the python package `MW-plot`. Documentation can be found in <https://milkyway-plot.readthedocs.io>.

tively. In total, 144 GCs are located at Galactocentric distances smaller than 20 kpc. As expected, a higher number of known GCs are located near the Sun in sector A. While roughly the same number of GCs are observed within Poisson errors (i.e., \sqrt{N}) in sectors B and D.

Assuming that the existing GCs are distributed isotropically, we can estimate the number of missing clusters in sector C by comparing it with the expected number of clusters observed on the near side of the MW. For both areas to be statistically similar (1σ errorbars), the number of missing clusters should be more than 12 and less than 26. Given the extensive observations on our side of the Galaxy (i.e., shaded area A), we can almost completely rule out the possibility of number variations in that sector (i.e., undiscovered GC near the Sun).

We repeated the above exercise by (1) counting only GCs currently located close to the plane ($|Z| < 1.5$ kpc) and (2) limiting $Z_{\text{max}} \leq 3.5$ kpc. The results give a similar number of ~ 11 -22 missing GCs. Adding previous estimations of missing GCs in the halo (Contenta et al. 2017; Webb & Carlberg 2021), the combined number of undiscovered clusters reaches up to a mean value of ~ 22 GCs ($(12+26)/2 = 19$ behind the Galactic bulge/bar/disk and 3 in the halo).

The number presented above represents a first approximation of the actual value, certainly affected by the violent dynamical processes dominating the early build-up history of the MW. In the more recent past of our Galaxy lifetime, only passages

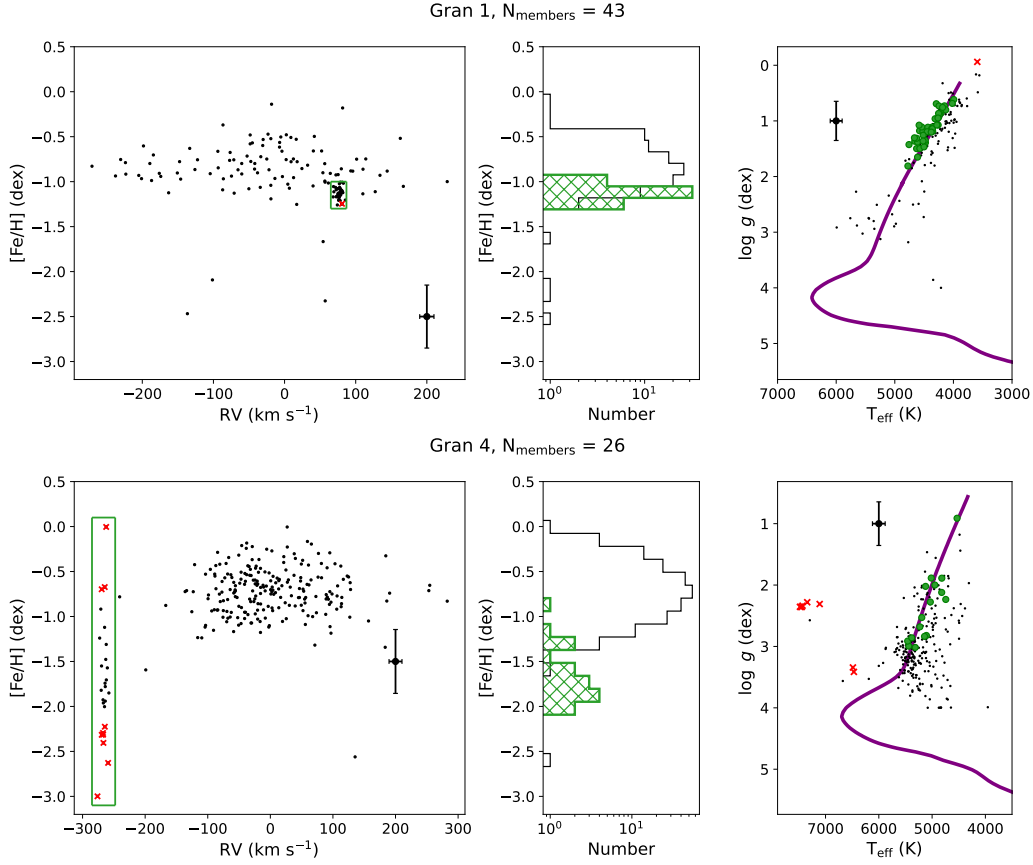


Fig. 2. **Left panels:** RV-[Fe/H] plane for all the MUSE extracted stars in the Gran 1 (**upper row**) and Gran 4 (**lower row**) fields. The box was drawn to select the cluster members using the individual RV and metallicity values. Red crosses represent stars outside the calibration parameter space, i.e., stars in the RGB tip or HB/SGB stars, which their RV coincides with the one derived for the cluster, but with no reliable stellar atmospheric parameter determination. **Middle panels:** Metallicity histogram for cluster selected stars. The highlighted hatched-filled histogram contains the cluster members with reliable metallicity measurements within the box. **Right panels:** Kiel diagram for the field and cluster stars in grey and green, respectively. A PARSEC isochrone was drawn using the same derived metallicity with an age of 10 Gyr. Number of members considers all the valid RV cluster stars, i.e., members within the highlighted box. The errorbar located in each panel represents the mean uncertainty for each corresponding parameter.

through the bar, the bulge and the disk might significantly affect the chance of survival of a GC.

4.2. Observational globular cluster mass limit across the Galaxy

Also relevant for the present discussion is the minimum cluster mass that a GC should have to survive and be detected nowadays. Obviously, the observed GC mass function varies dramatically from the inner MW to the distant halo. With only a few GCs missing in the halo, the detection threshold was pushed down to $\sim 10^3 M_\odot$ (see Madore & Arp 1982; Abell 1955; Carraro 2005). However, this is one order of magnitude smaller than the mass of the smallest GC detected towards the inner Galaxy.

Complex dynamical processes that occur within the Galaxy, including but not limited to two-body relaxation, tidal truncation, disk/bulge shocks, cluster mass loss, dynamical friction and changes in the Galactic potential, create this natural inner-to-outer mass difference (see Murali & Weinberg 1997; Baumgardt & Makino 2003; Kruijssen et al. 2012; Carlberg & Keating 2022; Ishchenko et al. 2023, and references therein). Most of the processes listed above occur when GCs are embedded in a dense environment or pass through the disk/bulge along their orbits. Recent dynamical analyses of GCs have been performed tak-

ing these processes carefully into account (e.g., Baumgardt et al. 2019a; Hughes et al. 2020; Ferrone et al. 2023), therefore, we can translate their results by searching for a lower limit on the GC bulge population.

Using the Baumgardt & Vasiliev (2021, March 2023 update) catalogue, we can construct Figure 5, that shows the initial and current GC masses for the entire MW GC population as a function of Galactocentric radius (R). A similar figure was presented in Baumgardt et al. (2019b, see their Fig. 7) but using the semi-major axis instead of R . Figure 5 includes also the maximum z extension (i.e., z_{\max}) as a colour-coded third dimension. We adopt an uncertainty of 25% of the cluster total mass (i.e., $\sigma_{\text{Current Mass}} = 0.25 \times M_{\text{Current}}$) in case mass uncertainties were missing in the catalogue.

Observationally, clear differences arise using R in the x-axis in this figure. First, it is easier to identify the bulge region using $R < 3.5$ kpc, as suggested by Rojas-Arriagada et al. (2020), and maybe extending up to ~ 6 kpc. In this area, as pointed out by Baumgardt et al. (2019b), dynamical processes determine a larger M_{initial} to M_{current} mass differences, as low-mass clusters ($\sim 10^4 M_\odot$) are more easily disrupted. The halo region also shows a distinct pattern, given the lower mass-loss of clusters and the lower mass observable limit of $\sim 10^3 M_\odot$ hitherto, possibly due to a different origin of these outer GCs.

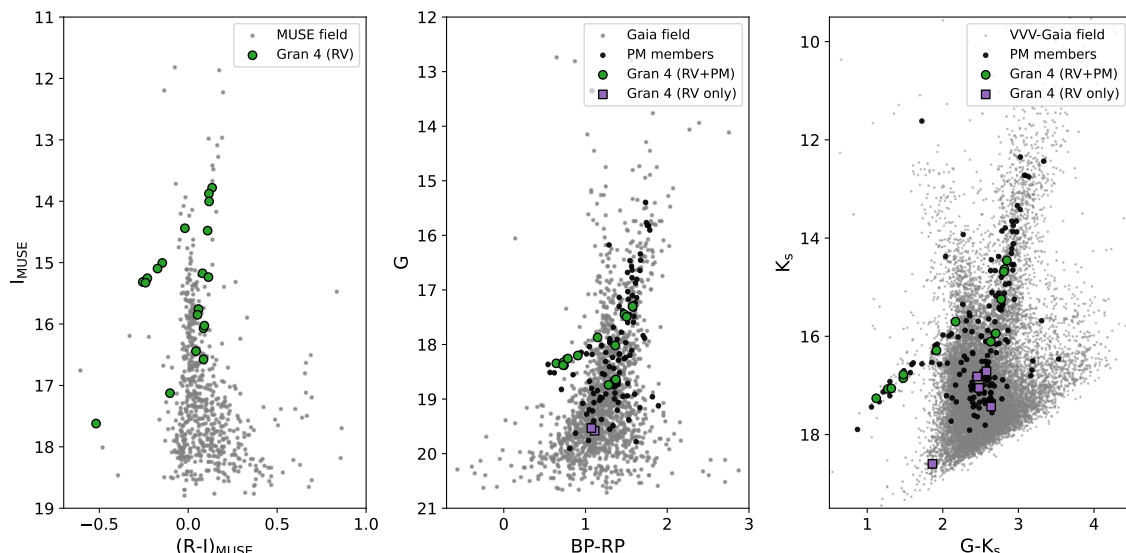


Fig. 3. CMDs of Gran 4 using different filters and catalogues. **Left panel:** MUSE CMD of the cluster, containing field stars in the MUSE field-of-view (background points) and cluster members selected by their RVs (green circles). **Middle panel:** Optical Gaia CMD comprising 2 arcmin within the cluster centre. Field stars are showed as background grey points, PM-cleaned members are showed in black points, RV and PM-selected cluster stars as green circles, while RV only members (i.e., faint to have PM measurements) are showed in purple squares. **Right panel:** Same as middle panel with an optical-near-IR CMD. Note that, for some stars, especially the faint-end, there are only measured BP nor RP-band magnitudes, resulting in a lower number of cluster stars in the CMDs.

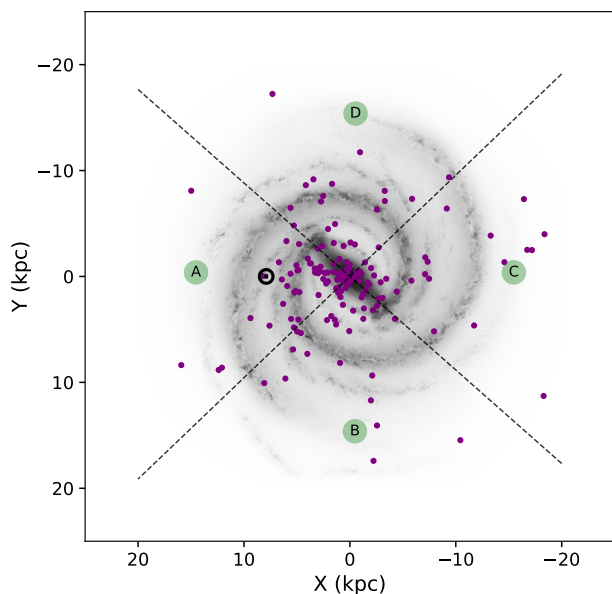


Fig. 4. Face-on artistic representation of the MW within the inner 20 kpc. The Sun is at (8, 0) kpc and the known GCs are indicated with \odot and purple filled circles, respectively. Reference lines are drawn to show the analysed areas (A, B, C and D), considering the Galactic bar as a symmetry axis (i.e., dashed line from top left to down right).

We can extend this analysis by including the newly discovered GCs and also extend the relationship to the Galactic disk, based on R . By comparing the mean mass loss shift from GCs at the same radius, we derive a rough estimate for the initial mass of Gran 4 to be $\sim 10^6 M_{\odot}$. Initial masses for the remaining clusters were already derived in the Baumgardt et al. (2019b) catalogue. A “bulge/disk disruption” region is hatched in grey in Figure 5, highlighting the observational lack of clusters. Note that this area

does not imply that GCs cannot exist in that part of the parameter space, only reveals that observations show no clusters in that area. A simple linear function $M(R) \sim 10^4 R^{-1} (M_{\odot} \text{ kpc}^{-1})$ was used to separate the parameter space in which GCs are observed. This functional form is valid from $R \sim 0.6$ kpc (Gran 1) until the edge of the MW disk at ~ 18 kpc (Gaia Collaboration et al. 2021), in which no GC has been observed below this threshold up to date.

5. Discussion and Conclusions

As a follow-up to our previous work (Gran et al. 2022), we have derived a mean radial velocity and metallicity for the cluster Gran 4 and updated the values derived for the Gran 1, 2, 3, and 5. Although we have analysed the same MUSE data as in Gran et al. (2022), we have now used the entire MUSE wavelength range rather than only two CaT lines, and we have also upgraded the PMs by using the Gaia DR3 catalogue.

Overall, we find an excellent agreement with previous studies of these clusters, with just a few key differences. Fernández-Trincado et al. (2022) derived a much lower metallicity for Gran 3 and a different RV for this cluster. We notice the same trend in the more recent study of Pace et al. (2023). This issue was corrected when re-analysing the MUSE spectra, due to an incorrect air-to-vacuum wavelength calibration used in Gran et al. (2022), which led to that discrepancy of $\sim 20 \text{ km s}^{-1}$ shift between our previous results and the Pace et al. (2023). Considering the metallicity dispersion, our derived RV and metallicity for Gran 3 (91.57 km s^{-1} and -1.63 dex, respectively, see Table 2), show remarkable similarity with the ones reported by Fernández-Trincado et al. (2022) (~ -1.7 dex and 95.9 km s^{-1}) and Pace et al. (2023) (-1.84 dex and 90.9 km s^{-1}). Finally, in the case of Gran 4, we derive a RV and metallicity of $[\text{Fe}/\text{H}] = -1.72$ dex and $\text{RV} = -265.3 \text{ km s}^{-1}$, respectively, which are compatible, within errors, with the ones derived in by Pace et al. (2023), i.e., $[\text{Fe}/\text{H}] = -1.84$ dex and $\text{RV} = -266.4 \text{ km s}^{-1}$. These values agree

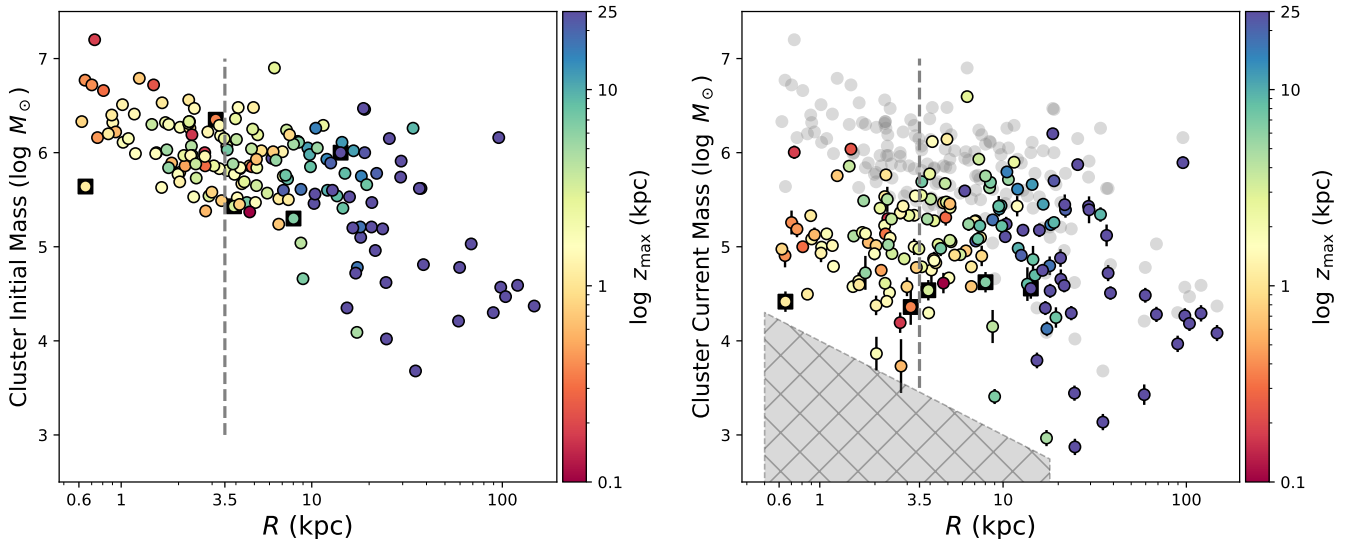


Fig. 5. Initial (left panel) and current (right panel) GC masses as a function of spherical Galactocentric radius (R), colour-coded by their Z_{\max} . The vertical line at 3.5 kpc is the estimated radius of the Galactic bulge. The grey hatched area in the right panel highlights the region where no GC has been discovered, implying an observational limit on the mass and orbital configuration below which GCs are more efficiently disrupted by the dynamical processes in the MW. The clusters analysed in this work are highlighted by squares in both panels. They are, in order of increasing R : Gran 1, 5, 3, 2, and 4. The right panel also contains the initial cluster masses derived by Baumgardt et al. (2019b) as grey background points, as a reference for the initial-to-final mass ratio of the GCs.

with the conclusions presented in Pace et al. (2023) of Gran 4 being part of the LMS/Wukong merger (Conroy et al. 2019; Naidu et al. 2020; Malhan et al. 2021) or the Helmi stream (Helmi et al. 1999).

Our analysis has proven that Gran 4 is a bonafide GC, previously hidden behind a highly crowded and reddened region towards the Galactic bulge. An initial mass of $\sim 10^6 M_{\odot}$ was assigned to the cluster based on the $M_{\text{initial}}/M_{\text{current}}$ ratio of clusters at similar Galactocentric radius. Furthermore, we present RVs and stellar atmospheric parameters for most of their observed members in a field-of-view of 1 sq arcmin from the centre. Future planned high-resolution follow-ups will disentangle whether or not the presented GCs host multiple stellar populations.

How many GCs are still missing on the far side of the Galaxy is still uncertain, and locating new GCs is challenging as a result of the high stellar density and reddening towards the Galactic bulge/plane. Despite our best estimation of $\sim 12-26$ GCs still to be discovered, the number heavily relies on critical assumptions like symmetry and cluster survival rate. However, substantial progress has been achieved in the last few years thanks to the release of the Gaia DR3 catalogue (Gaia Collaboration et al. 2022) and to the improvement in the performances of near-infrared detectors.

Recently, other stellar tracers have been used as well, shedding light on the spiral structure (Sanna et al. 2017; Minniti et al. 2020, 2021b), taking advantage of low-extinction windows (Saito et al. 2020), or using a variety of distance indicators (Hey et al. 2023) to map the other side of the Galaxy. GCs behind the bulge have been discovered and confirmed using joint observations, a number that will only increase with future Gaia DRs.

The promising new generation stellar surveys like WEAVE (Jin et al. 2023), 4MOST (de Jong et al. 2019; Lucatello et al. 2023), MOONS (Cirasuolo et al. 2020; Gonzalez et al. 2020), in addition to the augmented instrumental and observational capabilities of future facilities, e.g., Vera Rubin (Ivezić et al. 2019)

and Gaia-NIR (Hobbs et al. 2016), will significantly increase our overall understanding of the MW and its GCs, expanding well-observed clusters towards the plane.

Acknowledgements. We gratefully thank Patrick de Laverny for providing access to the AMBRE synthetic spectra. FG, GK and VH gratefully acknowledge support from the French National Research Agency (ANR) funded project “MWDisc” (ANR-20-CE31-0004) and “Pristine” (ANR-18-CE31-0017). This work was the last part of the Ph.D. thesis of FG, funded by grant CONICYT-PCHA Doctorado Nacional 2017-21171485. MZ acknowledges support from FONDECYT Regular grant No. 1230731. ARA acknowledges support from FONDECYT through grant 3180203. JAC-B acknowledges support from FONDECYT Regular No. 1220083. EV acknowledges the Excellence Cluster ORIGINS Funded by the Deutsche Forschungsgemeinschaft (DFG, German Research Foundation) under Germany’s Excellence Strategy – EXC-2094-390783311. Support for MZ, ARA, RC, and MDL is provided by the Ministerio de Ciencia, Tecnología, Conocimiento e Innovación/Agencia Nacional de Investigación y Desarrollo (ANID) Programa Iniciativa Científica Milenio through grant IC120009, awarded to the Millennium Institute of Astrophysics (M.A.S.) and the ANID BASAL Center for Astrophysics and Associated Technologies (CATA) through grant FB210003.

We gratefully acknowledge the use of data from the VVV ESO Public Survey program ID 179.B-2002 taken with the VISTA telescope, and data products from the Cambridge Astronomical Survey Unit (CASU). The VVV Survey data are made public at the ESO Archive. Based on observations taken within the ESO VISTA Public Survey VVV, Program ID 179.B-2002.

This work has made use of data from the European Space Agency (ESA) mission *Gaia* (<https://www.cosmos.esa.int/gaia>), processed by the *Gaia* Data Processing and Analysis Consortium (DPAC, <https://www.cosmos.esa.int/web/gaia/dpac/consortium>). Funding for the DPAC has been provided by national institutions, in particular the institutions participating in the *Gaia* Multilateral Agreement.

This research has made use of the VizieR catalogue access tool, CDS, Strasbourg, France (DOI: 10.26093/cds/vizier). The original description of the VizieR service was published in Ochsenbein et al. (2000). This research made use of: TOPCAT (Taylor 2005), IPython/Jupyter (Pérez & Granger 2007; Kluyver et al. 2016), numpy (Harris et al. 2020), matplotlib (Hunter 2007), Astropy, a community developed core Python package for Astronomy (Astropy Collaboration et al. 2013, 2018, 2022), Photutils, an Astropy package for detection and photometry of astronomical sources (Bradley et al. 2023), galpy: A Python Library for Galactic Dynamics (Bovy 2015), specutils (Earl et al. 2021), gala (Price-Whelan 2017; Price-Whelan et al. 2020), and Uncertainties: a Python package for calculations with uncertainties (Eric O. LEBIGOT, <http://pythonhosted.org/uncertainties/>). This research has made use of NASA’s Astrophysics Data System.

References

- Abell, G. O. 1955, *PASP*, 67, 258
- Arakelyan, N. R., Pilipenko, S. V., & Libeskind, N. I. 2018, *MNRAS*, 481, 918
- Astropy Collaboration, Price-Whelan, A. M., Lim, P. L., et al. 2022, *apj*, 935, 167
- Astropy Collaboration, Price-Whelan, A. M., Sipőcz, B. M., et al. 2018, *AJ*, 156, 123
- Astropy Collaboration, Robitaille, T. P., Tollerud, E. J., et al. 2013, *A&A*, 558, A33
- Bacon, R., Accardo, M., Adjali, L., et al. 2010, in *Society of Photo-Optical Instrumentation Engineers (SPIE) Conference Series*, Vol. 7735, *Ground-based and Airborne Instrumentation for Astronomy III*, ed. I. S. McLean, S. K. Ramsay, & H. Takami, 773508
- Bailin, J. 2019, *ApJS*, 245, 5
- Bailin, J. & von Klar, R. 2022, *ApJ*, 925, 36
- Bastian, N. & Lardo, C. 2018, *ARA&A*, 56, 83
- Baumgardt, H., Hilker, M., Sollima, A., & Bellini, A. 2019a, *MNRAS*, 482, 5138
- Baumgardt, H., Hilker, M., Sollima, A., & Bellini, A. 2019b, *MNRAS*, 482, 5138
- Baumgardt, H. & Makino, J. 2003, *MNRAS*, 340, 227
- Baumgardt, H. & Vasiliev, E. 2021, *MNRAS*, 505, 5957
- Bovy, J. 2015, *ApJS*, 216, 29
- Bradley, L., Sipőcz, B., Robitaille, T., et al. 2023, *astropy/photutils*: 1.8.0
- Bradley, L., Sipőcz, B., Robitaille, T., et al. 2022, *astropy/photutils*: 1.5.0
- Bragaglia, A. 2018, in *Astrometry and Astrophysics in the Gaia Sky*, ed. A. Recio-Blanco, P. de Laverny, A. G. A. Brown, & T. Prusti, Vol. 330, 119–126
- Bressan, A., Marigo, P., Girardi, L., et al. 2012, *MNRAS*, 427, 127
- Brodie, J. P. & Strader, J. 2006, *ARA&A*, 44, 193
- Callingham, T. M., Cautun, M., Deason, A. J., et al. 2022, *MNRAS*, 513, 4107
- Cantat-Gaudin, T. 2022, *Universe*, 8, 111
- Cantat-Gaudin, T. & Anders, F. 2020, *A&A*, 633, A99
- Cantat-Gaudin, T., Anders, F., Castro-Ginard, A., et al. 2020, *A&A*, 640, A1
- Cantat-Gaudin, T., Krone-Martins, A., Sedaghat, N., et al. 2019, *A&A*, 624, A126
- Carlberg, R. G. & Keating, L. C. 2022, *ApJ*, 924, 77
- Carraro, G. 2005, *ApJ*, 621, L61
- Castro-Ginard, A., Jordi, C., Luri, X., et al. 2020, *A&A*, 635, A45
- Castro-Ginard, A., Jordi, C., Luri, X., et al. 2022, *A&A*, 661, A118
- Castro-Ginard, A., Jordi, C., Luri, X., et al. 2018, *A&A*, 618, A59
- Choi, J., Conroy, C., Ting, Y.-S., et al. 2018, *ApJ*, 863, 65
- Cirasuolo, M., Fairley, A., Rees, P., et al. 2020, *The Messenger*, 180, 10
- Conroy, C., Bonaca, A., Cargile, P., et al. 2019, *ApJ*, 883, 107
- Contenta, F., Gieles, M., Balbinot, E., & Collins, M. L. M. 2017, *MNRAS*, 466, 1741
- Contreras Ramos, R., Zoccali, M., Rojas, F., et al. 2017, *A&A*, 608, A140
- de Jong, R. S., Agertz, O., Berbel, A. A., et al. 2019, *The Messenger*, 175, 3
- de Laverny, P., Recio-Blanco, A., Worley, C. C., et al. 2013, *The Messenger*, 153, 18
- de Laverny, P., Recio-Blanco, A., Worley, C. C., & Plez, B. 2012, *A&A*, 544, A126
- Earl, N., Tollerud, E., Jones, C., et al. 2021, *astropy/specutils*: v1.2
- Fernández-Trincado, J. G., Minniti, D., Garro, E. R., & Villanova, S. 2022, *A&A*, 657, A84
- Ferrone, S., Di Matteo, P., Mastrobuono-Battisti, A., et al. 2023, *A&A*, 673, A44
- Forbes, D. A., Bastian, N., Gieles, M., et al. 2018, *Proceedings of the Royal Society of London Series A*, 474, 20170616
- Forbes, D. A. & Bridges, T. 2010, *MNRAS*, 404, 1203
- Foreman-Mackey, D., Hogg, D. W., Lang, D., & Goodman, J. 2013, *PASP*, 125, 306
- Gaia Collaboration, Antoja, T., McMillan, P. J., et al. 2021, *A&A*, 649, A8
- Gaia Collaboration, Brown, A. G. A., Vallenari, A., et al. 2018, *A&A*, 616, A1
- Gaia Collaboration, Prusti, T., de Bruijne, J. H. J., et al. 2016, *A&A*, 595, A1
- Gaia Collaboration, Vallenari, A., Brown, A. G. A., et al. 2022, *arXiv e-prints*, arXiv:2208.00211
- Garro, E. R., Minniti, D., Alessi, B., et al. 2022a, *A&A*, 659, A155
- Garro, E. R., Minniti, D., Gómez, M., et al. 2020, *A&A*, 642, L19
- Garro, E. R., Minniti, D., Gómez, M., et al. 2022b, *A&A*, 662, A95
- Gonzalez, O. A., Mucciarelli, A., Origlia, L., et al. 2020, *The Messenger*, 180, 18
- Gran, F., Zoccali, M., Contreras Ramos, R., et al. 2019, *A&A*, 628, A45
- Gran, F., Zoccali, M., Saviane, I., et al. 2022, *MNRAS*, 509, 4962
- Gratton, R., Bragaglia, A., Carretta, E., et al. 2019, *A&A Rev.*, 27, 8
- Gratton, R., Sneden, C., & Carretta, E. 2004, *ARA&A*, 42, 385
- Hammer, F., Li, H., Mamon, G. A., et al. 2023, *MNRAS*, 519, 5059
- Harris, C. R., Millman, K. J., van der Walt, S. J., et al. 2020, *Nature*, 585, 357
- Harris, W. E. & Racine, R. 1979, *ARA&A*, 17, 241
- Hartke, J., Kakkad, D., Reyes, C., et al. 2020, in *Society of Photo-Optical Instrumentation Engineers (SPIE) Conference Series*, Vol. 11448, *Society of Photo-Optical Instrumentation Engineers (SPIE) Conference Series*, 114480V
- He, Z., Liu, X., Luo, Y., Wang, K., & Jiang, Q. 2023, *ApJS*, 264, 8
- He, Z., Wang, K., Luo, Y., et al. 2022, *ApJS*, 262, 7
- He, Z.-H., Xu, Y., Hao, C.-J., Wu, Z.-Y., & Li, J.-J. 2021, *Research in Astronomy and Astrophysics*, 21, 093
- Helmi, A., White, S. D. M., de Zeeuw, P. T., & Zhao, H. 1999, *Nature*, 402, 53
- Hey, D. R., Huber, D., Shappee, B. J., et al. 2023, *arXiv e-prints*, arXiv:2305.19319
- Hobbs, D., Høg, E., Mora, A., et al. 2016, *arXiv e-prints*, arXiv:1609.07325
- Huang, K.-W. & Koposov, S. E. 2021, *MNRAS*, 500, 986
- Hughes, M. E., Pfeffer, J. L., Martig, M., et al. 2020, *MNRAS*, 491, 4012
- Hunt, E. L. & Reffert, S. 2021, *A&A*, 646, A104
- Hunt, E. L. & Reffert, S. 2023, *A&A*, 673, A114
- Hunter, J. D. 2007, *Computing in Science & Engineering*, 9, 90
- Husser, T.-O., Latour, M., Brinchmann, J., et al. 2020, *A&A*, 635, A114
- Ishchenko, M., Sobolenko, M., Berczik, P., et al. 2023, *arXiv e-prints*, arXiv:2304.03547
- Ivezić, Z., Kahn, S. M., Tyson, J. A., et al. 2019, *ApJ*, 873, 111
- Jin, S., Trager, S. C., Dalton, G. B., et al. 2023, *MNRAS*[arXiv:2212.03981]
- Kluyver, T., Ragan-Kelley, B., Pérez, F., et al. 2016, in *Positioning and Power in Academic Publishing: Players, Agents and Agendas*, ed. F. Loizides & B. Schmidt, IOS Press, 87–90
- Koposov, S. E., Belokurov, V., & Torrealba, G. 2017, *MNRAS*, 470, 2702
- Kruijssen, J. M. D., Maschberger, T., Moeckel, N., et al. 2012, *MNRAS*, 419, 841
- Kruijssen, J. M. D., Pfeffer, J. L., Crain, R. A., & Bastian, N. 2019a, *MNRAS*, 486, 3134
- Kruijssen, J. M. D., Pfeffer, J. L., Reina-Campos, M., Crain, R. A., & Bastian, N. 2019b, *MNRAS*, 486, 3180
- Leaman, R., VandenBerg, D. A., & Mendel, J. T. 2013, *MNRAS*, 436, 122
- Lucatello, S., Bragaglia, A., Vallenari, A., et al. 2023, *The Messenger*, 190, 13
- Madore, B. F. & Arp, H. C. 1982, *PASP*, 94, 40
- Malhan, K., Yuan, Z., Ibat, R. A., et al. 2021, *ApJ*, 920, 51
- Marigo, P., Bressan, A., Nanni, A., Girardi, L., & Pumo, M. L. 2013, *MNRAS*, 434, 488
- Marín-Franch, A., Aparicio, A., Piotto, G., et al. 2009, *ApJ*, 694, 1498
- Massari, D., Koppelman, H. H., & Helmi, A. 2019, *A&A*, 630, L4
- Minniti, D., Fernández-Trincado, J. G., Smith, L. C., et al. 2021a, *A&A*, 648, A86
- Minniti, D., Geisler, D., Alonso-García, J., et al. 2017, *ApJ*, 849, L24
- Minniti, D., Lucas, P. W., Emerson, J. P., et al. 2010, *New A*, 15, 433
- Minniti, J. H., Sbordone, L., Rojas-Arriagada, A., et al. 2020, *A&A*, 640, A92
- Minniti, J. H., Zoccali, M., Rojas-Arriagada, A., et al. 2021b, *A&A*, 654, A138
- Murali, C. & Weinberg, M. D. 1997, *MNRAS*, 288, 749
- Myeong, G. C., Vasiliev, E., Iorio, G., Evans, N. W., & Belokurov, V. 2019, *MNRAS*, 488, 1235
- Naidu, R. P., Conroy, C., Bonaca, A., et al. 2020, *ApJ*, 901, 48
- Ness, M., Hogg, D. W., Rix, H. W., Ho, A. Y. Q., & Zasowski, G. 2015, *ApJ*, 808, 16
- Nidever, D. 2021, *dnidever/doppler*: Cannon and Payne models
- Ochsenbein, F., Bauer, P., & Marcout, J. 2000, *A&AS*, 143, 23
- Pace, A. B., Koposov, S. E., Walker, M. G., et al. 2023, *arXiv e-prints*, arXiv:2304.06904
- Pagnini, G., Di Matteo, P., Khoperskov, S., et al. 2022, *arXiv e-prints*, arXiv:2210.04245
- Pérez, F. & Granger, B. E. 2007, *Computing in Science and Engineering*, 9, 21
- Price-Whelan, A., Sipőcz, B., Lenz, D., et al. 2020, *adrn/gala*: v1.3
- Price-Whelan, A. M. 2017, *The Journal of Open Source Software*, 2
- Recio-Blanco, A. 2018, *A&A*, 620, A194
- Renzini, A. 2017, *MNRAS*, 469, L63
- Rojas-Arriagada, A., Zasowski, G., Schultheis, M., et al. 2020, *MNRAS*, 499, 1037
- Ryu, J. & Lee, M. G. 2018, *ApJ*, 863, L38
- Saito, R. K., Minniti, D., Benjamin, R. A., et al. 2020, *MNRAS*, 494, L32
- Sanna, A., Reid, M. J., Dame, T. M., Menten, K. M., & Brunthaler, A. 2017, *Science*, 358, 227
- Smith, L. C., Lucas, P. W., Kurtev, R., et al. 2018, *MNRAS*, 474, 1826
- Ströbele, S., La Penna, P., Arsenault, R., et al. 2012, in *Society of Photo-Optical Instrumentation Engineers (SPIE) Conference Series*, Vol. 8447, *Adaptive Optics Systems III*, ed. B. L. Ellerbroek, E. Marchetti, & J.-P. Véran, 844737
- Stuik, R., Bacon, R., Conzelmann, R., et al. 2006, *New A Rev.*, 49, 618
- Surot, F., Valenti, E., Hidalgo, S. L., et al. 2019, *A&A*, 623, A168
- Taylor, M. B. 2005, in *Astronomical Society of the Pacific Conference Series*, Vol. 347, *Astronomical Data Analysis Software and Systems XIV*, ed. P. Shopbell, M. Britton, & R. Ebert, 29
- Vanzella, E., Calura, F., Meneghetti, M., et al. 2017, *MNRAS*, 467, 4304
- Vasiliev, E. & Baumgardt, H. 2021, *MNRAS*, 505, 5978
- Wang, Z., Hayden, M. R., Sharma, S., et al. 2022, *MNRAS*, 514, 1034
- Watkins, L. L., van der Marel, R. P., Bellini, A., & Anderson, J. 2015, *ApJ*, 803, 29
- Webb, J. J. & Carlberg, R. G. 2021, *MNRAS*, 502, 4547
- Weilbacher, P. M., Palsa, R., Streicher, O., et al. 2020, *A&A*, 641, A28

**Appendix A: Appendix: additional GC plots and
complete membership catalogues**

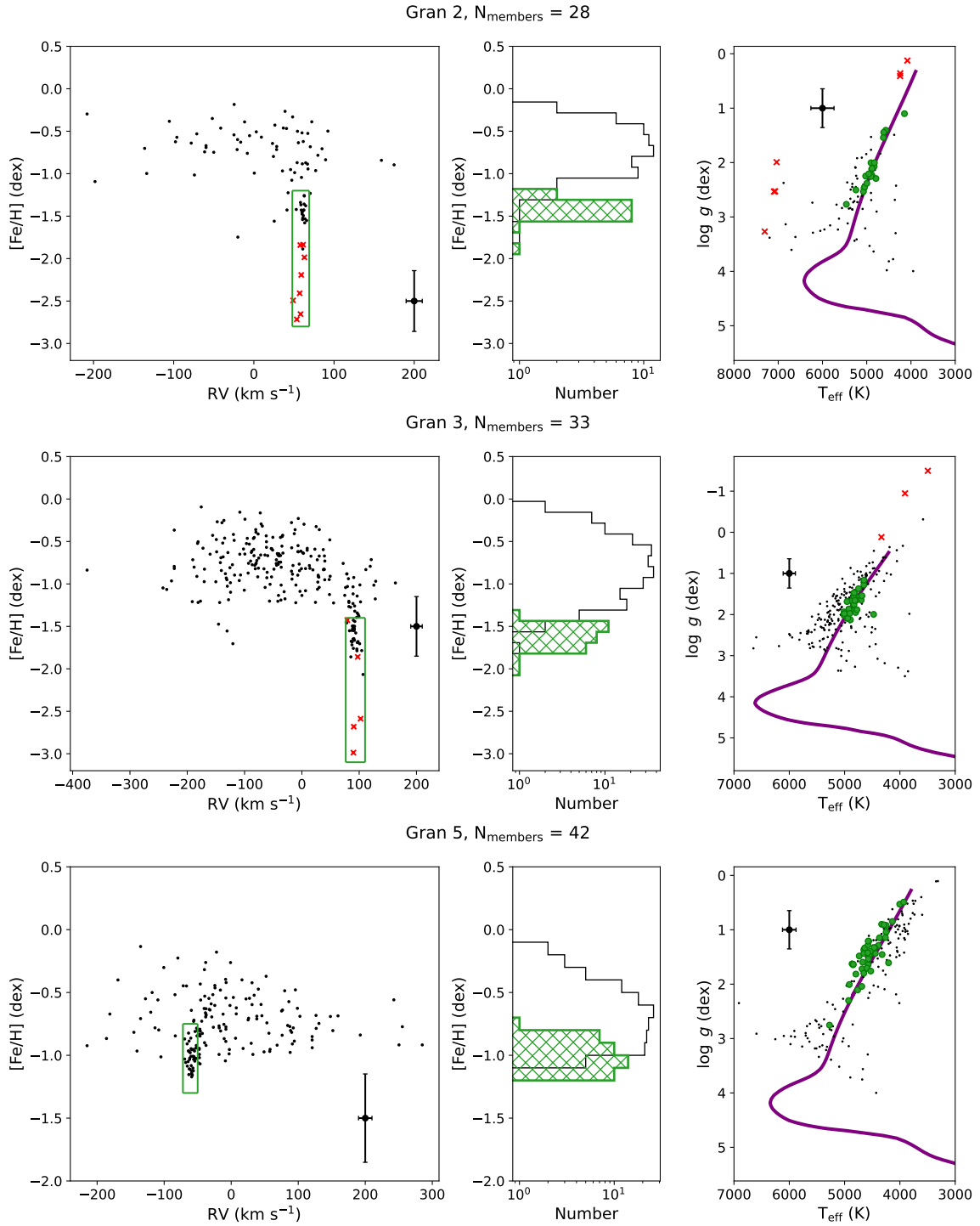


Fig. A.1. **Left panels:** RV-[Fe/H] plane for all the MUSE extracted stars in the Gran 2 (**upper row**), Gran 3 (**middle row**) and Gran 5 (**lower row**) fields. The box was drawn to select the cluster members using the individual RV and metallicity values. Red crosses represent stars outside the calibration parameter space, i.e., stars in the RGB tip or HB/SGB stars, whose RV coincides with that derived for the cluster, but with no reliable stellar atmospheric parameter determination. **Middle panels:** Metallicity histogram for cluster selected stars. Highlighted hatched-filled histogram contains the cluster members within the box. **Right panels:** Kiel diagram for the field and cluster stars in grey and green, respectively. A PARSEC isochrone was drawn using the same derived metallicity with an age of 10 Gyr. Number of members considers all the valid RV cluster stars, i.e., members within the highlighted box. The errorbar located in each panel represents the mean uncertainty for each corresponding parameter.

Table A.1. Atmospheric parameters for all the MUSE Gran 1 analysed stars. Star ID, coordinates, temperature, surface gravity, metallicity, RV, and mean SNR were derived for observed GC members based on their multidimensional membership (RV, [Fe/H], and Kiel diagram).

GC - ID	RA (deg)	Dec (deg)	T_{eff} (K)	$\log g$ (dex)	[Fe/H] (dex)	RV (km s ⁻¹)	SNR
Gran 01 - 008	269.64794	-32.02559	4362	1.2	-1.17	68.25	133
Gran 01 - 017	269.64650	-32.02449	4659	1.4	-1.11	69.33	174
Gran 01 - 021	269.65005	-32.02420	4358	1.1	-1.14	75.04	241
Gran 01 - 022	269.65615	-32.02395	4611	1.4	-1.05	68.81	222
Gran 01 - 027	269.66006	-32.02366	4577	1.2	-1.08	78.36	177
Gran 01 - 028	269.65463	-32.02359	4521	1.2	-1.17	76.71	185
Gran 01 - 031	269.65405	-32.02354	4416	1.2	-1.13	75.47	119
Gran 01 - 033	269.65832	-32.02317	—	—	—	80.74	371
Gran 01 - 034	269.65652	-32.02305	4540	1.1	-1.19	76.46	167
Gran 01 - 040	269.65639	-32.02255	4292	0.7	-1.26	74.18	64
Gran 01 - 041	269.65260	-32.02249	4153	0.7	-1.15	78.03	302
Gran 01 - 042	269.64663	-32.02239	4353	1.2	-1.13	77.38	121
Gran 01 - 044	269.64840	-32.02222	4627	1.5	-1.10	80.21	101
Gran 01 - 048	269.65071	-32.02198	4212	0.9	-1.12	81.96	293
Gran 01 - 056	269.65463	-32.02156	4131	0.8	-1.16	77.37	232
Gran 01 - 059	269.64769	-32.02121	4757	1.4	-1.02	82.67	168
Gran 01 - 061	269.64709	-32.02105	4776	1.8	-1.02	77.03	79
Gran 01 - 065	269.64866	-32.02094	4435	1.1	-1.06	77.35	106
Gran 01 - 066	269.65901	-32.02082	4245	0.7	-1.12	80.70	285
Gran 01 - 076	269.64899	-32.02021	4251	0.9	-1.09	72.58	198
Gran 01 - 082	269.66191	-32.01964	4572	1.5	-1.17	73.48	43
Gran 01 - 083	269.65417	-32.01947	3994	0.6	-1.17	77.06	313
Gran 01 - 087	269.64881	-32.01904	4477	1.4	-1.01	78.37	151
Gran 01 - 089	269.64552	-32.01901	4371	1.1	-1.15	78.18	139
Gran 01 - 090	269.65437	-32.01884	4358	1.1	-1.21	75.96	142
Gran 01 - 091	269.64879	-32.01884	4501	1.5	-1.01	81.11	143
Gran 01 - 095	269.65619	-32.01849	4447	1.2	-1.20	85.42	102
Gran 01 - 098	269.64272	-32.01788	4260	1.1	-1.09	78.35	80
Gran 01 - 102	269.64590	-32.01726	4627	1.3	-1.16	74.37	189
Gran 01 - 103	269.65461	-32.01716	4611	1.7	-1.15	78.97	83
Gran 01 - 104	269.65095	-32.01700	4233	0.9	-1.06	71.73	322
Gran 01 - 106	269.65882	-32.01693	4019	0.7	-1.13	77.90	267
Gran 01 - 107	269.65583	-32.01694	4481	1.3	-1.14	75.62	96
Gran 01 - 108	269.65208	-32.01644	4515	1.3	-1.08	74.41	163
Gran 01 - 113	269.65306	-32.01586	4253	0.9	-1.21	78.18	136
Gran 01 - 118	269.65076	-32.01565	4664	1.3	-1.08	75.08	161
Gran 01 - 126	269.65174	-32.01465	4378	1.2	-1.12	77.83	129
Gran 01 - 128	269.64577	-32.01443	4517	1.4	-1.17	72.40	93
Gran 01 - 129	269.64302	-32.01433	4282	1.1	-1.12	78.51	180
Gran 01 - 132	269.64382	-32.01395	4312	1.0	-1.25	80.51	141
Gran 01 - 140	269.65175	-32.01283	4184	0.8	-1.14	75.95	301
Gran 01 - 147	269.65825	-32.01144	4262	0.9	-1.11	81.18	191
Gran 01 - 151	269.64231	-32.01100	4584	1.1	-1.12	81.10	88

Table A.2. Atmospheric parameters for all the MUSE Gran 2 analysed stars. Star ID, coordinates, temperature, surface gravity, metallicity, RV, and mean SNR were derived for observed GC members based on their multidimensional membership (RV, [Fe/H], and Kiel diagram).

GC - ID	RA (deg)	Dec (deg)	T_{eff} (K)	$\log g$ (dex)	[Fe/H] (dex)	RV (km s ⁻¹)	SNR
Gran 02 - 004	257.89591	-24.85627	—	—	—	61.41	446
Gran 02 - 006	257.89126	-24.85582	—	—	—	57.91	357
Gran 02 - 016	257.89701	-24.85381	4903	2.0	-1.48	60.22	127
Gran 02 - 019	257.89022	-24.85292	4791	2.3	-1.42	52.90	250
Gran 02 - 021	257.89498	-24.85237	4883	2.2	-1.58	63.43	146
Gran 02 - 025	257.89939	-24.85186	5024	2.2	-1.55	65.79	146
Gran 02 - 026	257.89908	-24.85177	5244	2.5	-1.53	63.77	104
Gran 02 - 028	257.89909	-24.85161	5459	2.8	-1.36	62.70	82
Gran 02 - 034	257.89351	-24.85104	4887	2.1	-1.54	60.77	123
Gran 02 - 035	257.89755	-24.85093	5060	2.5	-1.34	58.15	67
Gran 02 - 036	257.89315	-24.85064	4905	2.3	-1.38	64.63	67
Gran 02 - 038	257.88808	-24.85059	—	—	—	58.22	103
Gran 02 - 041	257.89621	-24.85003	—	—	—	48.96	70
Gran 02 - 052	257.88781	-24.84909	—	—	—	57.16	221
Gran 02 - 053	257.88389	-24.84914	—	—	—	53.58	94
Gran 02 - 055	257.88941	-24.84859	5074	2.5	-1.26	62.84	53
Gran 02 - 060	257.89506	-24.84777	4831	2.1	-1.52	61.00	145
Gran 02 - 061	257.88843	-24.84776	4826	2.0	-1.37	58.69	65
Gran 02 - 063	257.89940	-24.84760	4569	1.4	-1.49	61.72	311
Gran 02 - 065	257.89433	-24.84742	—	—	—	59.09	110
Gran 02 - 074	257.89690	-24.84643	4616	1.4	-1.43	62.19	263
Gran 02 - 076	257.89143	-24.84603	4953	2.2	-1.43	59.16	121
Gran 02 - 088	257.88727	-24.84371	4623	1.5	-1.43	62.34	248
Gran 02 - 092	257.88665	-24.84299	4879	2.1	-1.45	60.43	112
Gran 02 - 093	257.89169	-24.84255	4146	1.1	-1.89	61.02	285
Gran 02 - 094	257.88905	-24.84238	5047	2.4	-1.46	60.14	139
Gran 02 - 095	257.89346	-24.84232	4997	2.4	-1.26	62.89	54
Gran 02 - 103	257.88298	-24.84043	—	—	—	63.04	299

Table A.3. Atmospheric parameters for all the MUSE Gran 3 analysed stars. Star ID, coordinates, temperature, surface gravity, metallicity, RV, and mean SNR were derived for observed GC members based on their multidimensional membership (RV, [Fe/H], and Kiel diagram).

GC - ID	RA (deg)	Dec (deg)	T_{eff} (K)	$\log g$ (dex)	[Fe/H] (dex)	RV (km s ⁻¹)	SNR
Gran 03 - 032	256.26735	-35.49913	4818	1.5	-1.52	91.34	73
Gran 03 - 034	256.25288	-35.49906	4822	1.9	-1.68	98.00	53
Gran 03 - 074	256.26345	-35.49795	4766	1.6	-1.50	91.92	71
Gran 03 - 091	256.25422	-35.49756	4850	1.7	-1.55	87.47	83
Gran 03 - 101	256.24863	-35.49737	—	—	—	90.49	214
Gran 03 - 152	256.25697	-35.49551	4868	1.7	-1.50	88.16	66
Gran 03 - 163	256.25260	-35.49513	4922	1.9	-1.65	89.46	111
Gran 03 - 169	256.26344	-35.49499	4949	2.1	-1.72	87.38	69
Gran 03 - 176	256.26352	-35.49485	4894	2.1	-1.86	85.48	76
Gran 03 - 189	256.26611	-35.49458	4831	1.6	-1.68	86.04	88
Gran 03 - 198	256.26460	-35.49447	4826	1.5	-1.76	89.79	109
Gran 03 - 204	256.25689	-35.49441	4800	2.0	-1.54	91.51	56
Gran 03 - 302	256.25186	-35.49234	4829	1.8	-1.58	94.05	67
Gran 03 - 334	256.24962	-35.49163	4698	1.6	-1.52	88.57	57
Gran 03 - 357	256.25547	-35.49105	4652	1.3	-1.68	87.76	118
Gran 03 - 362	256.25493	-35.49092	—	—	—	89.90	48
Gran 03 - 367	256.25521	-35.49079	4776	1.9	-1.49	89.72	52
Gran 03 - 397	256.26641	-35.49015	5010	2.0	-1.46	78.17	219
Gran 03 - 417	256.25740	-35.48946	4788	1.7	-1.79	96.10	114
Gran 03 - 448	256.25610	-35.48885	5009	1.9	-1.55	90.80	99
Gran 03 - 479	256.26517	-35.48813	4475	2.0	-2.07	106.77	68
Gran 03 - 485	256.25616	-35.48791	4748	1.4	-1.44	92.44	204
Gran 03 - 519	256.26526	-35.48692	—	—	—	79.33	211
Gran 03 - 533	256.25561	-35.48652	4955	1.7	-1.55	83.07	122
Gran 03 - 542	256.25971	-35.48608	4814	1.7	-1.69	96.64	111
Gran 03 - 551	256.26722	-35.48564	—	—	—	102.42	24
Gran 03 - 563	256.26245	-35.48517	4941	2.1	-1.70	100.79	111
Gran 03 - 567	256.26230	-35.48501	4907	2.0	-1.66	91.72	124
Gran 03 - 569	256.26380	-35.48497	4827	1.5	-1.43	89.73	100
Gran 03 - 584	256.25732	-35.48457	—	—	—	97.47	123
Gran 03 - 592	256.26850	-35.48423	4650	1.2	-1.64	90.75	188
Gran 03 - 600	256.25726	-35.48407	5006	2.0	-1.79	104.42	139
Gran 03 - 605	256.25759	-35.48387	4686	1.5	-1.77	95.87	51

Table A.4. Atmospheric parameters for all the MUSE Gran 4 analysed stars. Star ID, coordinates, temperature, surface gravity, metallicity, RV, and mean SNR were derived for observed GC members based on their multidimensional membership (RV, [Fe/H], and Kiel diagram).

GC - ID	RA (deg)	Dec (deg)	T_{eff} (K)	$\log g$ (dex)	[Fe/H] (dex)	RV (km s ⁻¹)	SNR
Gran 04 - 030	278.10913	-23.11954	—	—	—	-264.43	137
Gran 04 - 105	278.10611	-23.11620	—	—	—	-267.35	136
Gran 04 - 119	278.11364	-23.11583	—	—	—	-267.16	133
Gran 04 - 125	278.12205	-23.11561	5016	1.9	-1.93	-267.32	168
Gran 04 - 131	278.11607	-23.11537	4818	1.9	-1.94	-263.74	230
Gran 04 - 133	278.12187	-23.11533	4819	2.1	-1.55	-269.68	65
Gran 04 - 138	278.11595	-23.11512	5107	2.8	-1.71	-262.05	179
Gran 04 - 155	278.11657	-23.11421	—	—	—	-259.20	144
Gran 04 - 163	278.11162	-23.11389	—	—	—	-269.37	129
Gran 04 - 166	278.11517	-23.11376	4743	2.2	-2.00	-264.95	231
Gran 04 - 169	278.11323	-23.11371	—	—	—	-262.28	29
Gran 04 - 173	278.11554	-23.11356	4531	0.9	-1.24	-272.67	45
Gran 04 - 205	278.12211	-23.11244	—	—	—	-264.56	27
Gran 04 - 228	278.11179	-23.11137	5437	3.0	-1.85	-257.95	78
Gran 04 - 238	278.12152	-23.11100	5458	2.9	-1.12	-264.80	50
Gran 04 - 246	278.12139	-23.11054	5381	2.9	-1.48	-262.93	65
Gran 04 - 250	278.11547	-23.11050	—	—	—	-266.67	136
Gran 04 - 293	278.10536	-23.10850	—	—	—	-276.15	143
Gran 04 - 296	278.12011	-23.10823	5122	2.0	-0.92	-270.83	34
Gran 04 - 312	278.11662	-23.10762	5316	3.0	-1.57	-260.41	74
Gran 04 - 324	278.10822	-23.10686	5033	2.3	-1.31	-262.18	45
Gran 04 - 326	278.11352	-23.10683	5230	2.7	-1.74	-264.10	119
Gran 04 - 339	278.11269	-23.10611	—	—	—	-269.44	26
Gran 04 - 344	278.11325	-23.10594	4947	2.0	-1.96	-266.81	203
Gran 04 - 349	278.10683	-23.10553	5193	2.5	-1.82	-270.24	119
Gran 04 - 368	278.10652	-23.10461	5142	2.8	-1.78	-263.75	79

Table A.5. Atmospheric parameters for all the MUSE Gran 5 analysed stars. Star ID, coordinates, temperature, surface gravity, metallicity, RV, and mean SNR were derived for observed GC members based on their multidimensional membership (RV, [Fe/H], and Kiel diagram).

GC - ID	RA (deg)	Dec (deg)	T_{eff} (K)	$\log g$ (dex)	[Fe/H] (dex)	RV (km s ⁻¹)	SNR
Gran 05 - 027	267.22633	-24.17476	4846	1.6	-0.96	-63.81	236
Gran 05 - 029	267.22775	-24.17466	4915	2.0	-0.96	-58.90	68
Gran 05 - 035	267.22945	-24.17438	4136	0.8	-0.87	-69.43	134
Gran 05 - 036	267.22548	-24.17431	4865	1.6	-0.89	-62.80	281
Gran 05 - 042	267.22750	-24.17393	4248	0.9	-1.12	-59.38	247
Gran 05 - 044	267.22895	-24.17381	4444	1.4	-1.08	-59.68	185
Gran 05 - 049	267.22554	-24.17336	4652	1.4	-1.02	-61.75	269
Gran 05 - 057	267.23091	-24.17259	4563	1.2	-1.03	-62.12	233
Gran 05 - 058	267.22522	-24.17259	4249	1.0	-0.85	-51.03	55
Gran 05 - 061	267.22553	-24.17243	4534	1.4	-1.10	-57.10	102
Gran 05 - 067	267.22840	-24.17209	4388	1.3	-1.05	-64.24	64
Gran 05 - 068	267.23760	-24.17204	4369	1.1	-1.01	-59.89	232
Gran 05 - 069	267.23280	-24.17170	4684	1.7	-0.81	-50.32	44
Gran 05 - 073	267.22329	-24.17153	4634	1.3	-0.97	-54.73	347
Gran 05 - 078	267.22841	-24.17116	4003	0.5	-1.05	-54.28	474
Gran 05 - 081	267.23992	-24.17094	4261	1.1	-0.94	-52.70	80
Gran 05 - 084	267.22811	-24.17060	4454	1.3	-1.03	-56.04	76
Gran 05 - 088	267.23146	-24.17020	4573	1.6	-1.11	-62.53	110
Gran 05 - 089	267.22906	-24.17015	4763	2.1	-1.12	-56.42	113
Gran 05 - 100	267.22622	-24.16938	4330	0.9	-1.15	-59.29	250
Gran 05 - 104	267.22273	-24.16927	4927	2.3	-0.82	-63.61	121
Gran 05 - 106	267.23644	-24.16894	4735	1.5	-0.98	-61.20	226
Gran 05 - 110	267.22883	-24.16858	4688	2.0	-1.01	-57.12	87
Gran 05 - 112	267.23578	-24.16848	4555	1.5	-1.11	-61.57	128
Gran 05 - 116	267.23394	-24.16831	4287	0.9	-1.15	-63.20	254
Gran 05 - 119	267.22347	-24.16813	4568	1.5	-1.16	-57.94	103
Gran 05 - 120	267.23420	-24.16809	4672	1.6	-1.03	-51.75	166
Gran 05 - 129	267.22876	-24.16765	4652	1.8	-1.03	-69.44	124
Gran 05 - 131	267.22614	-24.16760	4575	1.3	-1.01	-55.48	55
Gran 05 - 137	267.23877	-24.16681	4842	1.6	-0.95	-59.93	232
Gran 05 - 156	267.23577	-24.16442	4573	1.2	-0.95	-56.62	367
Gran 05 - 160	267.22267	-24.16432	4595	1.7	-1.02	-53.59	144
Gran 05 - 161	267.23078	-24.16419	4535	1.4	-0.92	-52.07	284
Gran 05 - 162	267.22791	-24.16421	4652	1.4	-0.97	-63.20	240
Gran 05 - 167	267.22864	-24.16359	4796	1.8	-1.06	-67.82	66
Gran 05 - 176	267.22931	-24.16247	4466	1.3	-0.91	-65.73	41
Gran 05 - 177	267.22653	-24.16249	4204	1.6	-0.81	-53.90	103
Gran 05 - 178	267.22700	-24.16242	4321	1.5	-0.86	-60.25	226
Gran 05 - 179	267.23139	-24.16237	4581	1.4	-1.09	-65.49	53
Gran 05 - 180	267.22852	-24.16232	5272	2.8	-0.78	-51.57	147
Gran 05 - 183	267.22476	-24.16209	4527	1.8	-1.17	-58.93	141
Gran 05 - 188	267.22261	-24.16170	3931	0.5	-1.14	-58.94	422